Quantum mechanical studies of helium atom scattering from isolated CO molecules on metal surfaces

2002 J. Phys.: Condens. Matter 14 6263

(http://iopscience.iop.org/0953-8984/14/24/318)

INSTITUTE OF PHYSICS PUBLISHING JOURNAL OF PHYSICS: CONDENSED MATTER

J. Phys.: Condens. Matter **14** (2002) 6263–6280 PII: S0953-8984(02)37189-3

Quantum mechanical studies of helium atom scattering from isolated CO molecules on metal surfaces

Sven Nave and Didier Lemoine

Laboratoire de Physique des Lasers, Atomes et Molécules, UMR CNRS 8523,
Centre d'Etudes et de Recherches Lasers et Applications, Université de Lille 1, Bâtiment P5,
59655 Villeneuve d'Ascq Cedex, France

E-mail: Didier.Lemoine@univ-lille1.fr

Received 17 June 2001
Published 31 May 2002
Online at stacks.iop.org/JPhysCM/14/6263

Abstract

We review two distinct quantum mechanical theories of atomic scattering from a point defect, single adsorbate or vacancy, inducing a corrugation much larger than that of the crystal surface. They are both based upon unrestricted motion of the probe and involve a realistic interaction potential. The most sophisticated one is a pseudospectral wavepacket method that is presented in both Cartesian and cylindrical representations. The physically attractive, albeit more approximate, close-coupling gas phase approach is also considered. We report the first realistic comparison with the experimental measurements of helium atom scattering on CO/Cu(100), at a beam energy of 20 meV. The combined use of the gas phase and of the reference models enables the unambiguous interpretation of all experimental peaks.

1. Introduction

The first attempts to characterize the angular distribution of helium atom scattering (HAS) from single adsorbates were the seminal, theoretical studies of Yinnon *et al* [52] and of Heuer and Rice [20], which predicted interference patterns whose analysis could provide a wealth of information on the adsorbate geometry and interaction, in comparison with a conventional specular beam attenuation study that only yields global versus detailed properties. The first experimental observations of these interference patterns are due to Lahee *et al* [29] for CO/Pt(111), 15 years ago. Toennies and co-workers followed up with high-resolution measurements for CO either on Cu(100) [4, 18] or on Pt(111) [8]. In the experiments the diffraction signal from the bare metal surface is always found to be negligible and in addition, at a low, few per cent CO coverage, the in-plane scattering interference patterns do not vary appreciably relative to the beam azimuthal angle. Thereby, the metal surface corrugation can be ignored in the process

under study. Time-of-flight (TOF) analysis at a few selected geometries revealed that the scattering is dominated by the elastic channel. It was also shown in the first experiments that the interference peak positions remain unaffected while increasing the crystal sample temperature. Moreover, the sample temperature could be lowered to 50 K in the two last experiments, thus reducing inelastic scattering processes. One further step was achieved in the last experiment on CO/Pt(111), for which full TOF measurements were performed in order to separate the elastic from the inelastic contributions (see the beautiful series of spectra in figure 1 of [8]). Yet, the scattering intensities are sensitive to most experimental parameters, and obviously to the details of the interaction between He and the chemisorbed molecule/metal system. Considering that nowadays state-of-the-art *ab initio* computations are not accurate enough to determine the interaction potential for He scattering from such a complex system, especially in the van der Waals (VdW) region, it is hopeless at present to reproduce the scattering intensities. The available experimental data have motivated a number of modelling studies aiming at interpreting the interference patterns [4, 6, 8, 10, 11, 18, 29, 35, 46, 48, 53]. All of these studies consistently made the approximations of a flat metal surface and of a rigid adsorbate/substrate system, and focused on reproducing the interference maximum positions in the angular distribution as a function of momentum transfer and of beam energy. As a result, all scattering mechanisms most likely to contribute were established, for example diffraction and reflection symmetry interferences (RSIs) [29], surface-induced rainbows [53] and gas-phase-like rainbows [35]. In addition, it was found to be crucial to resort to a fully quantum treatment of HAS [53], with unrestricted, three-dimensional motion of the probe [6] and for a realistic, attractive He–CO potential [35]. Still, it is not clear whether surface-induced rainbows or RSI actually contribute under the experimental conditions and depending on beam energy. Indeed, the three crucial requirements have not been fulfilled in a quantitative comparison with the experiments, apart from the recent study of CO/Pt(111) by Choi *et al* [8], who however assume a hard metal wall and use a pure gas phase potential, thus ignoring any surface-specific rainbow and any distortion mechanism from the van der Waals metal interaction. One reason is that the experimental distributions are recorded by rotating the sample in the scattering plane, with the source and detector kept at a fixed angle θ_{SD}, hence defining as many distinct pairs of incidence (θ_i) and scattering (θ_f) angles as angular recordings, and thus as many three-dimensional simulations in a quantum scattering approach involving a realistic surface interaction. The problem would become even more intricate in order to model the inelastic distributions. Yet, this difficulty was circumvented by Choi *et al* [9], who attempted to map the inelastic contributions from the measured elastic angular distribution for CO/Pt(111), owing to a simple theory of form factors.

The object of this paper is to first review two distinct quantum mechanical strategies, both based upon unrestricted motion of the atomic probe and involving a realistic interaction potential, and to then report the first realistic theory–experiment comparison for the CO/Cu(100) system. Following previous studies we make the approximations of a flat metal surface and of a rigid adsorbate/substrate system. Section 2 gives the details of the interaction potential. The best, albeit numerically expensive, strategy is a three-dimensional pseudospectral wavepacket method that is presented in section 3, in both Cartesian *and* cylindrical representations. The theory more generally applies to atomic scattering from a point defect, single adsorbate or vacancy, inducing a corrugation much larger than that of the crystal surface. Application to He scattering from CO/Cu(100) under normal incidence serves as a description of the contributing mechanisms and of their energy dependence, based on past interpretations. The physically attractive, albeit more approximate, close-coupling gas phase approach is considered in section 4. Section 5 focuses on the comparison with the experimental measurements on CO/Cu(100) at a beam energy of 20 meV, and furthermore gives the unambiguous interpretation of all experimental peaks owing to the combined use of the gas phase and of the reference models.

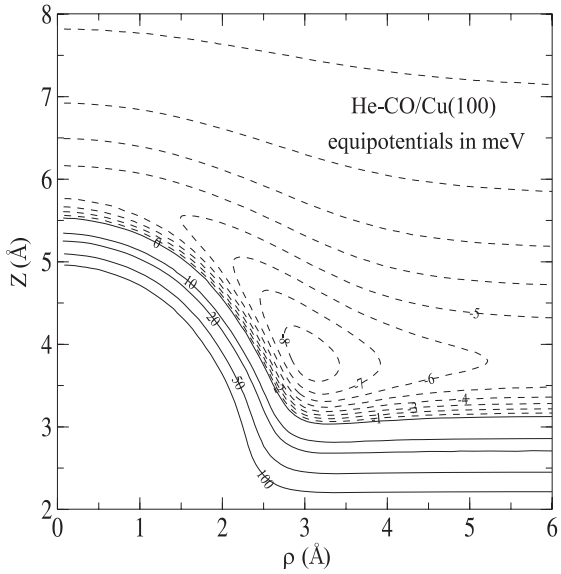

Figure 1. Potential energy contours in meV for in-plane He scattering from CO adsorbed on Cu(100), based on the *ab initio* He–CO study of Heijmen *et al* [19]. CO lies along the z axis at $\rho = 0$. The solid (0, 10, 20, 50, 100) equipotentials reflect the repulsive interaction whereas the dashed $[-8, -1]$ ones represent the attractive region.

2. Interaction potential

CO is known to adsorb at top sites of Cu(100) in the collinear sequence Cu–C–O with $d_{\mathrm{CuC}} = 1.9 \pm 0.1$ Å and $d_{\mathrm{CO}} = 1.15 \pm 0.1$ Å (see [14] and references therein). The measure of the CO separation does not differ from the equilibrium value of 1.13 Å found in the gas phase with sophisticated *ab initio* techniques [19]. Furthermore, no detectable He diffraction peak could be observed for the bare Cu(100) [14]. Therefore, the interaction potential for He scattering from an isolated CO adsorbate can be expressed as the sum $V(\boldsymbol{R}) = V_{\mathrm{He–CO}}(\boldsymbol{R} - \boldsymbol{R}_{\mathrm{CO}}) + V_{\mathrm{He–Cu(100)}}(z)$, involving a gas phase He–CO potential and the interaction of He with Cu(100) assumed to be flat. $\boldsymbol{R} = (x, y, z)$ and $\boldsymbol{R}_{\mathrm{CO}} = (0, 0, z_{\mathrm{CO}})$ denote the position vectors of He and of the CO centre of mass, respectively; z is the He–surface distance and $\rho = \sqrt{x^2 + y^2}$ is the lateral He–CO distance. Two distinct gas phase potentials are considered, namely the old one from Thomas, Kraemer and Diercksen (TKD) [51] and the most recent one from Heijmen *et al* [19]. Following Ellis *et al* [14], the He–surface interaction relies on the Chizmeshya–Zaremba potential [7] and on the Tang–Toennies van der Waals damping function $f_2(x) = 1 - \mathrm{e}^{-x}(1 + x + \frac{x^2}{2})$ [50], thus defining

$$V_{\mathrm{He–Cu(100)}}(z) = V_0(1 + \gamma z)\mathrm{e}^{-\gamma z} - \frac{C_{vdW}}{(z - z_{vdW})^3} f_2\left[\left(\gamma - \frac{\gamma}{1 + \gamma z}\right)(z - z_{vdW})\right]$$

with $V_0 = 1.487$ eV, $\gamma = 2.718$ Å^{-1}, $C_{vdW} = 0.227$ eV Å^3 and $z_{vdW} = 0.171$ Å. The He–surface potential is translated from z to $z - z_B - z_{shift}$ in order to account for the jellium edge–surface distance $z_B = 0.814$ Å and for a shift of the origin, which was found useful by Ellis *et al* to improve their fit with respect to the TKD potential. One should keep in mind that in terms of HAS angular distributions, setting a nonzero value to z_{shift} is equivalent to varying z_{CO} by the same amount. z_{CO} is set to the effective CO island height of 2.3 Å derived by Ellis *et al*, which tends to be slightly too small relative to the experimental values of d_{CuC}

and d_{CO}. Nonetheless, in view of the simplicity of the potential modelling, that is assuming that the gas phase interaction is not distorted by the surface interaction, an adjustable parameter is needed to locate CO with respect to the calculated He–surface potential and z_{shift} is just as good as any other choice. z_{shift} is the *only* adjustable parameter that will be used in our studies. Figure 1 displays a contour plot of the He–CO/Cu(100) potential generated with the gas phase interaction of Heijmen *et al* and $z_{shift} = 0$.

3. Pseudospectral wavepacket method

The time-dependent Schrödinger equation is solved with the initial wavefunction consisting of the product of a Gaussian wavepacket, $G(z)$, for the probe motion normal to the surface,

$$G(z) = (2\pi\sigma^2)^{-1/4} \exp\left(-\frac{(z - z_0)^2}{4\sigma^2}\right) \exp(\mathrm{i}k_{z_0} z), \tag{1}$$

and of a plane wave for its parallel motion, $P(\boldsymbol{\rho}) = \exp(\mathrm{i}\boldsymbol{k}_{\rho_i}\boldsymbol{\rho})/A^{-1/2}$. A is the effective beam area and $\boldsymbol{k}_{\rho_i}$ is the incident momentum parallel to the surface. z_0 and σ are the average location and halfwidth (standard deviation) of $G(z)$, and k_{z_0} its average momentum. $G(z)$ is positioned in the asymptotic region and its momentum distribution corresponds to a wavepacket impinging on the surface. The Hamiltonian operator for a probe of mass M, is the sum of the kinetic energy operator, $\boldsymbol{T} = -\hbar^2 - \Delta/2M$, that is diagonal in the $\boldsymbol{K} = (k_x, k_y, k_z)$ momentum space, and of the potential energy operator, $\boldsymbol{V}$, that is diagonal in the $\boldsymbol{R}$ coordinate space. The scattering wavefunction is expanded and propagated in a truncated momentum representation that is a finite set of the orthonormal eigenfunctions of the Laplacian operator, and thus diagonal asymptotically. The pseudospectral or orthogonal collocation approach [16, 17] consists in setting up the isomorphic transformation between the truncated momentum representation and a discrete coordinate representation (DCR), in which $\boldsymbol{V}$ is *assumed* diagonal. This assumption is minimized by the Gaussian quadrature underlying the discrete orthogonal transform and backtransform steps. The failure of this assumption is better known as 'aliasing' and can be avoided by augmenting the grid density in the DCR. In Cartesian coordinates the pseudospectral approach implied by the Laplacian eigenfunctions, is the well known Fourier method [24, 25, 41].

3.1. Cartesian representation (x, y, z)

The Laplacian eigenfunctions are three-dimensional direct products of normalized Fourier functions defined as $\Phi_m^F(u) = \exp(\mathrm{i}k_{u_m}u)/\sqrt{L_u}$, on a segment L_u along $u = x, y, z$, with eigenvalues $-k_{u_m}^2$. The finite basis size, N_u, defines discrete Fourier transforms (DFTs)

$$F_{m\alpha}^{u\dagger} = \frac{\exp(-\mathrm{i}k_{u_m}u_\alpha)}{\sqrt{N_u}} = \sqrt{\omega_\alpha}\Phi_m^{F\star}(u_\alpha) \tag{2}$$

with equal weights and/or spacings $\omega_\alpha = \Delta u = L_u/N_u$ in the DCR. The trapezoidal rule underlying the DFT is of order $2N_u - 1$ for plane wave expansions [16, 17, 41] and relates to a Gauss–Chebychev quadrature [13, 42]. An additional asset is that the Fourier method can exploit the fast Fourier transform (FFT) algorithm to perform the requested DFTs [15–17, 23].

$A = L_xL_y$ would be equivalent to the surface unit cell in a conventional atom–crystal interaction, but since the CO defect breaks the periodicity of the surface, it must correspond to a surface mesh, $\boldsymbol{\rho}_{\alpha\beta} = (\alpha\Delta x, \beta\Delta y)$, the area beyond which the scattering contribution is purely specular relative to the CO-induced angular distribution. The radial symmetry of the interaction model suggests $L_x = L_y$ and $N_x = N_y$, with $-N_x/2 \leqslant \alpha, \beta \leqslant N_x/2$. Following Kroes and

Mowrey [28], the shifting theorem of Fourier analysis is used to treat any arbitrary angle of incidence. Simply, rather than Fourier expanding around $\boldsymbol{k}_\rho = (k_x = 0, k_y = 0)$, the parallel momentum mesh, $\boldsymbol{k}_{\rho_{mn}} = (k_{x_m}, k_{y_n})$, is centred around $\boldsymbol{k}_\rho = \boldsymbol{k}_{\rho_i}$, both along x and y, with Fourier spacings $\Delta k = 2\pi/L_x$. Since the momentum representation is our primary representation and since we are not concerned with any property of the wavefunction in the DCR, the $\exp(\pm \mathrm{i}\boldsymbol{k}_{\rho_i}\boldsymbol{\rho}_{\alpha\beta})$ shifting and backshifting steps required within the DCR [28] can just be ignored. In addition to straightforwardly selecting the θ_i value of choice, this technique optimizes the momentum sampling at non-normal incidences. Furthermore, defining the scattering plane perpendicular to y, the reflection symmetry with respect to $k_y = 0$ or $y = 0$ can be exploited by applying fast cosine transforms (FCTs) [5] in the symmetry-adapted cosine momentum basis or DCR of size $N_{x_s} = N_x/2 + 1$, instead of full FFTs along y [31]. When $N_x \gg 1$, as is the case here, the FCT scheme reduces by a factor of two both the overall three-dimensional grid size and the execution time, apart from some additional overhead associated with the FCT.

The scattering wavefunction is evolved in time via the second-order split operator propagator (SOP) of Feit *et al* [15] owing to the following symmetric partitioning of the time evolution operator:

$$\boldsymbol{U}(\Delta t) \approx \exp\left(-\mathrm{i}\frac{\boldsymbol{T}(\boldsymbol{K})\Delta t}{2\hbar}\right)\boldsymbol{F}^{z\dagger}\boldsymbol{C}^{y}\boldsymbol{F}^{x\dagger}\exp\left(-\mathrm{i}\frac{\boldsymbol{V}(\boldsymbol{R})\Delta t}{\hbar}\right)\boldsymbol{F}^{x}\boldsymbol{C}^{y}\boldsymbol{F}^{z}\exp\left(-\mathrm{i}\frac{\boldsymbol{T}(\boldsymbol{K})\Delta t}{2\hbar}\right) \quad (3)$$

with DFT matrices $\boldsymbol{F}^u$ defined in equation (2), and where $\boldsymbol{C}^{\boldsymbol{y}}$ designates the discrete cosine transform along y, which is its own inverse [5]. Under normal incidence an FCT scheme can also replace the FFT scheme along x and the reflection symmetry with respect to $k_y = k_x$ or $y = x$ can be further exploited by working with a symmetry-needed grid of size $[N_{x_s}(N_{x_s}+1)]/2$ that is smaller than a full two-dimensional Fourier grid, by a factor of eight when $N_x \gg 1$ [31]. Although the SOP is much less sensitive to the spectral range spanned by the $\boldsymbol{H}$ operation than for example the Chebychev propagator [49], it is useful to apply an energy cut-off, E_{max}, to both the maximum potential [15] and kinetic [25] energies. Since parallel momentum transfer is very efficient in the present case and since the largest anisotropy occurs along z at the repulsive wall, whereby aliasing is more probable than along x or y, it is appropriate to choose $E_{max} = E_{z_{max}}$, which should be a good cut-off overestimate. As in [33, section 3.5], the energy cut-off also defines the number of 'active' $\boldsymbol{k}_\rho$ states, that is for $E_x + E_y \leqslant E_{max}$, thus reducing the labour associated with the transforms along z and with the kinetic energy multiplications. A simplified asymptotic treatment [30, 33] within the Chebychev scheme can also be adapted to the SOP. Within the $\boldsymbol{K}$-primary representation there is no need to explicitly transform the wavefunction in the $\{x, y\}$ DCR in the asymptotic region, that is for $z \geqslant z_\infty$, since the potential coupling must be negligible. One only needs to precompute the diagonal matrix elements of $\boldsymbol{V}$ in the mixed (k_x, k_y, z) representation, which are straightforwardly given by the two-dimensional trapezoidal rule as

$$\overline{V}(z \geqslant z_\infty) = \frac{1}{N_x^2}\sum_{\alpha=1}^{N_x}\sum_{\beta=1}^{N_x} V(\rho_{\alpha\beta}, z), \quad (4)$$

and its SOP components $S^V_{mnmn}(z) = \exp(-\mathrm{i}\frac{\overline{V}(z\geqslant z_\infty)\Delta t}{\hbar})$ that supersede $\boldsymbol{S}^V(z) = \boldsymbol{C}^y\boldsymbol{F}^{x\dagger}\exp(-\mathrm{i}\frac{\boldsymbol{V}(\boldsymbol{R})\Delta t}{\hbar})\boldsymbol{F}^x\boldsymbol{C}^y$ for $z \geqslant z_\infty$ in equation (3). This results in diagonal multiplications for the potential energy operation for $z \geqslant z_\infty$, which represents a negligible numerical cost in comparison with the FCT/FFT savings. The savings are significant since the x and y transform lengths are much larger than the z one because of the lack of mesh periodicity, and thus computationally much more expensive. We use the estimate $z_\infty = \min(z_0 - \sigma, z_f)$

as both the initial wavepacket and the flux analysis performed at z_f (see below) should lie in the negligible-potential-coupling region.

In order to limit the extent of the spatial representation the outgoing wavefunction is absorbed near the grid edge at large positive z. One way to do this is to apply splitting functions after each time step when the atomic probe recedes into the asymptotic region [26]. Alternatively, one can introduce an optical potential in the absorbing region [27]. In the context of the second-order SOP the two techniques are equivalent [44]. However, within the $\boldsymbol{K}$-primary representation the first technique requires an additional pair of FFTs along z at each time step. Therefore, we use an optical potential which we choose to be of cubic form, i.e.

$$V_{opt}(z > z_f) = -\mathrm{i}\varepsilon\left(\frac{z - z_f}{L_{opt}}\right)^3$$

where $L_{opt} = z_{N_z} - z_f$, with strength (ε) and length (L_{opt}) parameters optimized with respect to the outgoing energy range and according to some error criterion [47]. In complement to the absorbing procedure a floating grid [33, 37, 38] along z can be used to bring the wavepacket into the interaction region in a first stage, and to achieve a minimal grid extent when absorption is turned on in the second stage. Once the absorbing procedure is started $V_{opt}(z > z_f)$ is added to $\overline{V}(z \geqslant z_\infty)$, and a flux analysis [12, 54] is performed at z_f, just ahead of the absorption zone. The width of $G(z)$ (cf equation (1)) defines the energy range available for post-collisional analysis. The energy-resolved probability for the probe to scatter with parallel momentum $\boldsymbol{k}_{\rho_{mn}}$ is calculated as

$$P_{mn}(E) = \frac{\hbar}{M}\frac{1}{[G(E)]^2}\mathrm{Im}\left[\psi^{\star}_{mn}(z_f, E)\left(\frac{\mathrm{d}\psi_{mn}(z, E)}{\mathrm{d}z}\right)_{z=z_f}\right]$$

involving the Fourier transform of the time-dependent coefficients of the parallel momentum representation at z_f

$$\psi_{mn}(z_f, E) = \int_0^\infty \psi_{mn}(z_f, t)\exp(\mathrm{i}Et)\,\mathrm{d}t$$

and a similar transform for the derivative of the wavefunction at z_f, which can be expressed owing to its Fourier representation

$$\frac{\mathrm{d}\psi_{mn}(z, t)}{\mathrm{d}z} = \boldsymbol{D}^z\psi_{mn}(z, t) = [\boldsymbol{F}^z(\mathrm{i}\boldsymbol{k}_z)\boldsymbol{F}^{z\dagger}]\psi_{mn}(z, t).$$

Applying FFTs back and forth is a brute force method that computes the derivative for all z grid points. The most accurate and efficient way is to precalculate the row of the derivative matrix for the flux analysis point from the analytical expressions derived by Meyer [41], i.e. $D^z_{ff} = 0$,

$$D^z_{fi\neq f} = (-1)^{i-f}\frac{2\pi}{L_z}\left(2f_{circ}\left[\frac{(\mathrm{i} - f)\pi}{N_z}\right]\right)^{-1}$$

and to perform the row-vector multiplication for each desired $\boldsymbol{k}_\rho$ state. f_{circ} is the circular sine (tangent) function for an odd (even) number of grid points along z. The flux formalism yields probabilities without phase resolution and is therefore, when used in conjunction with the absorption procedure, the analysis method that can optimally limit the extent of the z grid. Within the $\boldsymbol{K}$-primary representation it amounts to FFTing each desired $\boldsymbol{k}_\rho$ component along z after each time step. This is however much less numerical work in comparison with all the savings enabled by the $\boldsymbol{K}$-primary representation choice. Furthermore, since the $\boldsymbol{K}$ representation is the asymptotic representation it is simplest to set up the initial wavepacket, i.e. $G(z)$ is placed in the specular channel and all other channels are zeroed out, and no (x, y)

transformations are necessary for the flux analysis as would be the case within the DCR-primary representation. Moreover, the flux analysis can be restricted to the asymptotically open channels, and even further for the problem under study, by only considering the in-plane scattering momentum states. Then, the flux computation is really negligible.

Before proceeding any further the SOP versus the reference Chebychev propagator choice can be briefly explained. The pseudospectral wavepacket approach should scale linearly with the number of Hamiltonian operations. This is the case in our implementations within either the Cartesian or cylindrical representation. To illustrate the SOP efficiency we are using the 'model I' three-dimensional application of Carré and Lemoine [6], who published the most involved calculations on the subject until the present work. A time step $\Delta t = 40$ fs was found to be small enough to reproduce the angular distribution to the desired accuracy of two to three digits. Thereby, the SOP calculation needed 4.2 (4.5) times fewer Hamiltonian operations than for an equivalent global Chebychev time propagation with a relative expansion truncation error of $10^{-7}(10^{-14})$. Since the absorbing procedure and the flux analysis are optimally limiting the extent of the grid and of the time propagation, the global Chebychev propagation is not appropriate. The Chebychev propagation should then be split into several time steps, small enough to ensure proper time sampling for the flux analysis as well as stability of the scheme in the presence of an optical potential [27], and would thus lead to an increased total number of Hamiltonian operations. Nevertheless, a gain by a factor > 4 is already impressive. In addition the SOP memory requirements are also more favourable.

3.2. Cylindrical representation (ρ, ϕ, z)

The radial symmetry of the interaction model (i.e. $V(\boldsymbol{R}) = V(\rho, z)$ does not depend on ϕ because CO stands upright) is then fully described. Following Persson and Jackson [45] and Lemoine and Jackson [38], the scattering wavefunction can be written as the partial-wave expansion

$$\Psi(\boldsymbol{R}, t) = \sum_{\nu=-\infty}^{+\infty} c_\nu \psi^\nu(\rho, z, t) \frac{\exp(\mathrm{i}\nu\phi)}{\sqrt{2\pi}} \tag{5}$$

and the two-dimensional plane wave $P(\boldsymbol{\rho})$ is expanded in cylindrical waves to find

$$\psi^\nu(\rho, z, t = 0) = \frac{\mathrm{i}^\nu}{c_\nu} \sqrt{\frac{2\pi}{A}} J_\nu(k_{\rho_i}) G(z)$$

where $J_\nu(k_{\rho_i}\rho)$ is a Bessel function of the first kind. Absorbing boundary conditions are enforced at $\rho = L$, implying $J_\nu(k_{\rho_i} L) = 0$ and $A = \pi L^2$. The c_ν coefficients are chosen to normalize the radial part of each ψ^ν independently. They can be deduced analytically by applying the orthogonality property of the Bessel functions and a recurrence relation to evaluate the resulting derivative [32, see equations (12), (13)], thereby yielding

$$c_\nu^2 = \frac{2}{L^2} \int_0^L J_\nu^2(k_{\rho_i}\rho)\rho \, \mathrm{d}\rho = J_{\nu+1}^2(k_{\rho_i} L)$$

so a normalized Bessel function [32, equation (13)] is obtained for the ρ dependence. By symmetry only the $\nu \geqslant 0$ partial waves need to be considered. The boundary condition also implies that k_{ρ_i} and L cannot be chosen independently. Since $k_{\rho_i} = \frac{\sqrt{2ME}}{\hbar} \sin\theta_i$ is an initial beam condition L has to be varied as a function of ν (see [38, section 2 and 3.3]). The details of the discrete Bessel methodology can be found elsewhere [32, 34, 38]. Only the main aspects will be mentioned here.

ψ^ν is expanded in terms of the Laplacian eigenfunctions, that is a direct product of a Fourier function $\Phi_l^F(z)$ and of a normalized Bessel function expressed as $\Phi_{j\nu}^B(\rho) = n_{j\nu} J_\nu(k_{\rho_j}\rho)$ with

$n_{j\nu} = \sqrt{2}/|LJ_{\nu+1}(s_{j\nu})|$, where $s_{j\nu}$ is the jth nonzero zero of J_ν and $k_{\rho_j}L = s_{j\nu}$, and with eigenvalue $-k^2_{\rho_j}$. The finite basis size, N_ρ, defines symmetric discrete Bessel transforms (DBTs)

$$B^\nu_{j\alpha} = n_{\alpha\nu}n_{j\nu}J_\nu(k_{\rho_j}\rho_\alpha) = \sqrt{\omega_\alpha}\Phi^B_{j\nu}(\rho_\alpha) \tag{6}$$

with $n_{\alpha\nu} = \sqrt{2}/|KJ_{\nu+1}(s_{\alpha\nu})|$, where $K\rho_\alpha = s_{\alpha\nu}$ and $KL = s_{N_\rho+1}$ [32, 34]. By analogy with the Fourier method the $(\rho_\alpha, \omega_\alpha = n^2_{\alpha\nu})$ set characterizes the Bessel quadrature underlying each DBT, which has been shown to be of Gaussian accuracy [32, 34]. Actually, these DBTs are nearly but not exactly orthogonal. However, they can be orthogonalized very easily [34]. Moreover, the difference between results stemming from near-orthogonal and orthogonalized DBTs has always been found to be negligible in previous bound-state calculations [34] and Eley–Rideal reactions [38], or in the present study. Accordingly, we preserve the same DBT notation in the following although the results presented hereafter are performed with orthogonalized DBTs, since the orthogonalization procedure involves a negligible precomputation time [34].

According to the partial-wave expansion of equation (5), each ψ^ν is propagated independently with the $\boldsymbol{K}$-based second-order SOP translated as

$$\boldsymbol{U}_\nu(\Delta t) \approx \exp\left(-\mathrm{i}\frac{\boldsymbol{T}_\nu(\boldsymbol{K})\Delta t}{2\hbar}\right)\boldsymbol{F}^{z\dagger}\boldsymbol{B}^\nu \exp\left(-\mathrm{i}\frac{V(\boldsymbol{R})\Delta t}{\hbar}\right)\boldsymbol{B}^\nu\boldsymbol{F}^z \exp\left(-\mathrm{i}\frac{\boldsymbol{T}_\nu(\boldsymbol{K})\Delta t}{2\hbar}\right) \tag{7}$$

with DBT matrices $\boldsymbol{B}^\nu$ defined in equation (6), and where $\boldsymbol{T}_\nu$ includes the Laplacian $(\nu/\rho)^2$ term singular at the origin. Whereas the DBT does not rely on a fast algorithm it resolves analytically the $\rho = 0$ singularity which proves to prevail in terms of accuracy and grid size [32, 34], especially for $\nu = 0$ and 1.

The simplified asymptotic treatment amounts to precomputing the diagonal matrix elements of $\boldsymbol{V}$ in the mixed (k_ρ, z) representation for $z \geqslant z_\infty$. The counterpart of equation (4) is now given by the Bessel quadrature as

$$\overline{V_{jj}}^\nu(z \geqslant z_\infty) = \sum_{\alpha=1}^{N_\rho} B^\nu_{j\alpha}V(\rho_\alpha, z)B^\nu_{j\alpha},$$

and is used to precalculate the SOP components $S^V_{jj}(z) = \exp(-\mathrm{i}\frac{\overline{V_{jj}}^\nu(z\geqslant z_\infty)\Delta t}{\hbar})$ that supersede $\boldsymbol{S}^V(z) = \boldsymbol{B}^\nu \exp(-\mathrm{i}\frac{V(\boldsymbol{R})\Delta t}{\hbar})\boldsymbol{B}^\nu$ for $z \geqslant z_\infty$, in equation (7). Although the treatment applies to one versus two dimensions the savings remain significant because the DBT multiplications take most of the computation time. The energy cut-off, absorbing procedure, floating grid technique and flux analysis are similar to those used in the Cartesian representation, except that the time-dependent coefficients of the parallel momentum representation now read $\psi^\nu_j(z, t)$. However, two more steps are required, that is the projection onto plane wave states and the summation over all the contributing partial waves. Furthermore, the k_{ρ_j} grids are ν dependent and a delicate interpolation procedure is needed. Moreover, the lack of a shifting theorem for the Bessel expansion makes the off-normal incidence calculations less flexible. Indeed, in order that k_{ρ_i} matches a k_{ρ_j} grid point one has to vary L accordingly and to make sure that the L value is satisfactory regarding both the boundary condition and the N_ρ sampling. In order to compare with the experiments it is necessary to sample large incidence angles that will imply a large partial-wave expansion and, thus, a series of tedious calculations, even though these are fast in terms of computation. Therefore, we choose to forego the Fourier–Bessel representation for the off-normal-incidence calculations.

3.3. Normal-incidence application

Under normal incidence the cylindrical partial-wave expansion reduces to the $\nu = 0$ contribution, so the task is greatly simplified and the projection onto plane-wave states is straightforward. Hence, the cylindrical representation can be most efficiently used in this case. This can also help a lot with defining appropriate values for a number of parameters for off-normal-incidence purposes without the trouble of a thorough three-dimensional Fourier convergence study. In order to compare with the Cartesian representation one needs to set $L = L_x/2$ and $N_\rho = N_{x_s}$. All other parameters are similar to those in the Cartesian representation. We used $N_z = 96$ and $N_\rho = 145$. Figure 2 compares the angular distributions calculated for a beam energy of 20 meV and the interaction potential shown in figure 1, within the cylindrical, three-and two-dimensional Cartesian representations. The three-dimensional Fourier distribution is superimposed on the two-dimensional Fourier–Bessel with the exception of the slight differences for the largest ΔK momentum transfers. This large-ΔK region corresponds to receding velocities that are quite slow or even too slow for the probe to escape from the He–Cu(100) potential well. This grazing-exit-angle region is very difficult to describe since it would necessitate a very long propagation time *and* a quasi-infinite absorption length to account for the huge associated de Broglie wavelengths. Furthermore, both the scattering and potential models are too simplistic to provide a realistic description in this situation since any small effect, whether it comes from the present potential accuracy or for example from missing metal corrugation and phonons, not mentioning any kind of defect and the lateral interaction with other CO adsorbates, will strongly affect the large-ΔK region. Nonetheless, the agreement between the three-dimensional Fourier and Fourier–Bessel curves is still very good in this region and perfect for most of the distribution. This demonstrates the accuracy of the cylindrical representation, which is even expected to be the highest since it relies on two- versus three-dimensional simulations. In contrast the two-dimensional Fourier curve strongly disagrees, both quantitatively and qualitatively. As noted previously [6], in analogy with optical diffraction one would replace a two-dimensional hole of radius L with a one-dimensional slit of length $2L$, and observe a same level of disagreement for $\Delta K < 3$ Å^{-1}. In the large-ΔK region the disagreement is no longer qualitative since it corresponds to surface-induced rainbows that can be traced to inflection points in the adsorbate equipotential of the classical turning point, that is at the collision energy probed [53]. Indeed, because of the radial symmetry of the scattering model the inflection points and the deviation angles are similar whether or not the probe motion is restricted to a plane.

Carré and Lemoine [6] have analysed the HAS energy dependence for a model CO/Pt(111) system. Such an analysis is reported in figure 3 for a higher energy range and the interaction potential shown in figure 1. The near-specular hump (R_0) that evolves into a shoulder at higher energies is a rainbow maximum induced by the He–adsorbate van der Waals forces [35, 39]. The next two oscillations (F_1, F_2) are Fraunhofer diffraction peaks [29]. The next, broad bimodal structure results from the competition of two distinct mechanisms. The first maximum may either be a third Fraunhofer peak or the single-collision rainbow manifestation. This rainbow effect classically occurs at the ripple present at low equipotential values, in the vicinity of the adsorbate [53]. Since the ripple is visible in the 3–3.5 Å radial range of figure 1, and in analogy with the previous findings on the model CO/Pt(111) system, we incline to the single-collision rainbow interpretation. This could be inferred from a classical analysis such as performed by Yinnon, Kosloff and Gerber [53]. The second maximum of the broad structure and all the remaining oscillations are double-collision rainbow effects including supernumerary structures appearing at increasing energies (R_1, R_2, R_3, ...). One of the two impacts classically occurs at an inflection point in the adsorbate equipotential at the probe energy [53]. As explained above,

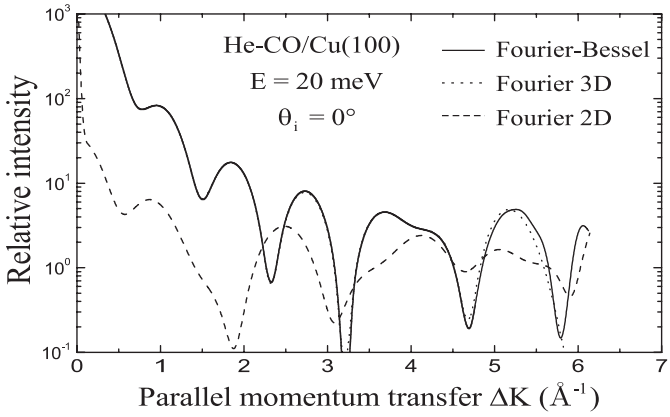

Figure 2. Log-scale plot of the angular distribution of He scattering from CO adsorbed on Cu(100), under normal incidence, at a collision energy of 20 meV. The solid curve depicts the result obtained within the cylindrical representation whereas the dotted and dashed curves refer to the three-and two-dimensional Cartesian representations.

the very end of the angular distribution should not be given a precise meaning. It is noteworthy that the R_0 and Fraunhofer maximum positions are fixed relative to ΔK, whereas the large-ΔK rainbow maximum positions shift outward with increasing energy.

4. Close-coupling gas phase approach

The two independent studies of Jónsson *et al* [22] and of Heuer and Rice [20] were the first to explicitly draw a parallel between the atomic scattering from single adsorbates and atom–molecule scattering in the gas phase. By assuming an underlying flat surface and enforcing the vanishing boundary condition along the mirror plane, the atom–adsorbate scattering can be formulated as the interference of two gas phase collision events, i.e. the so-called RSI. The reflection construction forms a virtual molecule by extending the probe–adsorbate interaction by symmetry with respect to the mirror plane [20, 22]. In gas phase scattering the angular distribution is conveniently referred to as the differential cross section (DCS), defined as the square of the scattering amplitude [20, 39, 43]. The scattering amplitude for the atom–adsorbate scattering, F, is expressed in terms of those for the atomic scattering with the virtual molecule, f, that is

$$F(\boldsymbol{k}_f, \boldsymbol{k}_i) = f(\boldsymbol{k}_f \cdot \boldsymbol{k}_i) - f(\boldsymbol{k}_f \cdot \boldsymbol{k}_s), \tag{8}$$

where $\boldsymbol{k}_i, \boldsymbol{k}_f, \boldsymbol{k}_s$ designate the incident, final and specular momentum vectors. $f(\boldsymbol{k}_f \cdot \boldsymbol{k}_i)$ describes the direct scattering from the adsorbate whereas $f(\boldsymbol{k}_f \cdot \boldsymbol{k}_s)$ accounts for the probe specularly reflected from the mirror surface, before or after hitting the adsorbate. This gas phase approach has been pursued by Manson, Toennies and co-workers [18, 29] within the hard-wall approximation. It was later implemented by Lemoine [35] for both hard and soft potentials, thereby revealing that the first interference peak in the angular distribution is a rainbow maximum arising from the van der Waals interaction between the probe and the adsorbate [39]. Recently, a similar approach has been proposed by Choi *et al* [8, 11]. Lemoine [36] has demonstrated the equivalence between their analytical derivation and that of Heuer and Rice [20], for a hard-hemisphere model. Because the same boundary condition and reflection symmetry are exploited it is expected that the equivalence between the two

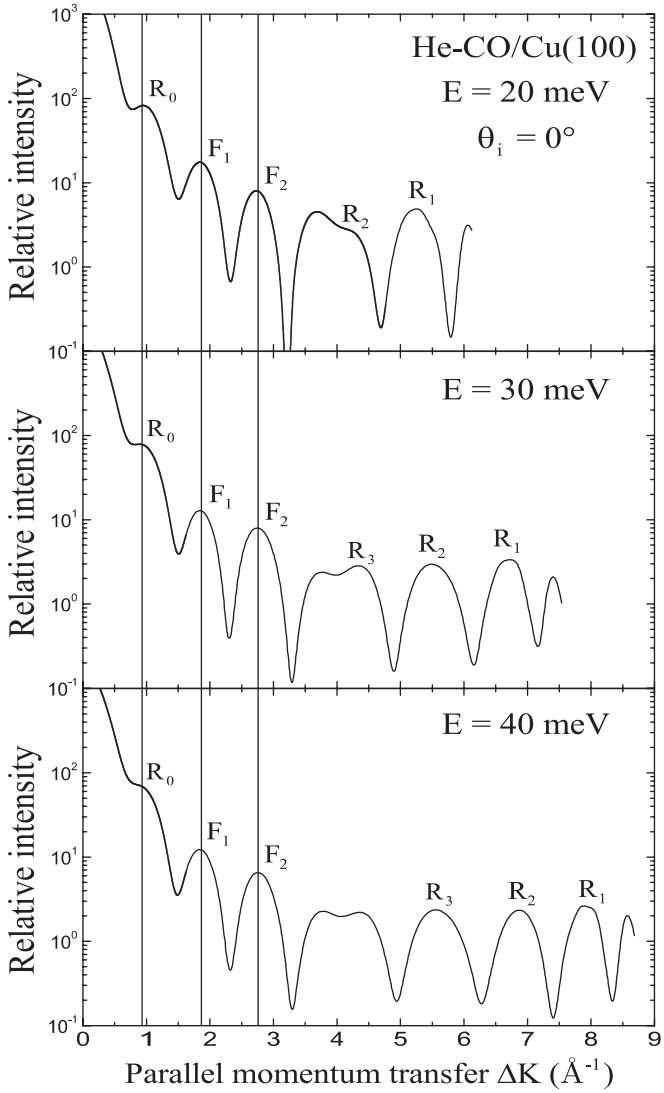

Figure 3. Log-scale plot of the angular distribution of He scattering from CO adsorbed on Cu(100), under normal incidence, at collision energies of 20, 30 and 40 meV from top to bottom panel. F_i labels a Fraunhofer oscillation and R_i a rainbow structure. The vertical lines indicate the steadiness of the R_0 and Fraunhofer maximum positions.

formulations subsists for a realistic, attractive He–CO potential. Yet, the earlier formulation is simpler and furthermore represents the direct application of the reflection symmetry. Moreover, the gas phase formulation enables the straightforward use of a number of available close-coupling scattering packages, without the need to implement a specific code for it. Indeed, the time-independent close-coupling approach is very well suited to treating rotationally inelastic collisions between an atom and a rigid rotor. Since standard close-coupling techniques have been well known for quite a long time, we shall not describe them here. We rather refer the reader to the efficient propagation algorithms of Manolopoulos and Alexander [2, 40], which we have resorted to in this study, and to the references therein.

Under the experimental in-plane scattering conditions with $\theta_{SD} = \theta_i + \theta_f = 95.8°$, the RSI amplitude of equation (8) reads

$$F(\theta_i) = f(\pi - \theta_{SD}) - f(|\theta_{SD} - 2\theta_i|). \tag{9}$$

The DCS angular dependence is well characterized in the gas phase [39, 43], giving rise to rainbow and diffraction oscillation patterns (see also figure 1 of [3] for an instructive comparative series of total DCS for scattering of He off Ar, O_2, NO and N_2). Forward scattering dominates, especially in the near-elastic (specular relative to the surface) range. Therefore, the direct scattering from the adsorbate, i.e. $f(\pi - \theta_{SD})$ in equation (9), only contributes as a constant, and the dominant near-specular scattering originates from the double-collision event, $f(|\theta_{SD} - 2\theta_i|)$ in equation (9).

The probe interaction with the virtual molecule is obtained from the reflection construction [8, 20, 22]. The mirror plane should locate the repulsive wall of the probe–substrate interaction, outward with respect to the surface plane. The position of the adsorbate centre of mass above the mirror plane, z_{ma}, plays the same role as the adjustable z_{shift} parameter in the reference model. If $\boldsymbol{R}_m = \boldsymbol{R} - \boldsymbol{R}_{\mathrm{CO}} + \boldsymbol{R}_{ma} = (x, y, z_m = z - z_{\mathrm{CO}} + z_{ma})$ denotes the probe position vector with respect to the origin at the mirror plane, lying directly below or above CO, the interaction potential for the virtual molecule is defined as

$$V_{\mathrm{He}-aa}(\boldsymbol{R}_m) = \begin{cases} V_{\mathrm{He-CO}}(\rho, z_m - z_{ma}) & \text{if } z_m \geqslant 0 \\ V_{\mathrm{He-CO}}(\rho, -z_m - z_{ma}) & \text{if } z_m < 0 \end{cases} \tag{10}$$

where 'aa' reflects the fact that the adsorbate interaction probed by the scatterer generates one half of the virtual homonuclear molecule. The adsorption of CO on Cu(100) implies that He probes predominantly the O end of the CO molecule, and that equation (10) induces an interaction potential that is intermediate to the He–O–C and He–O_2 scattering cases. A schematic view of the reflection construction and of the classical RSI trajectories deflected by $V_{\mathrm{He}-aa}$ is provided in figure 4. $V_{\mathrm{He}-aa}$ is represented by a few energy contours calculated from the He–CO potential of Heijmen *et al* [19], with $z_{ma} = 0$.

5. Comparison with the experiment

Similar to the normal-incidence simulations we used a three-dimensional ($96 \times 145 \times 288$) grid size in the pseudospectral calculations. In order to compare with the experiment the angular distribution was sampled every 0.07 Å^{-1} with respect to parallel momentum transfer $\Delta K = k_i(\sin(\theta_{SD} - \theta_i) - \sin\theta_i)$, according to the allowed (θ_i, θ_f) range. Following Ellis *et al* [14], the TKD He–CO potential was considered with $z_{shift} = 0.64$ Å. However, the comparison with the HAS experimental measurements of Graham *et al* [18] on the CO/Cu(100) system, at a beam energy of 20 meV, yields a TKD-based angular distribution that is significantly squeezed and shifted inward with respect to the specular scattering. In order to make up for this z_{shift} would have to be much increased, up to a quite unrealistic value. Therefore, the TKD potential was dropped and the most recent He–CO potential of Heijmen *et al* [19] was then used to generate all angular distributions shown in this work. The comparison, at a beam energy of 20 meV, is displayed in figure 5, for both $z_{shift} = 0$ and 0.16 Å. Only the angular range including identifiable maxima besides Bragg peaks in the experimental distribution is shown. The vertical arrows point to the positions of the absolute experimental maxima and also pass through the calculated interference peaks. With $z_{shift} = 0$ the agreement on the maximum positions is very good, considering that the experimental oscillations are not sharply peaked and that the arrows do not point to the bump centres. The dashed curve illustrates the sensitivity to the z_{shift} parameter for which a variation of +0.16 Å slightly shifts the oscillatory

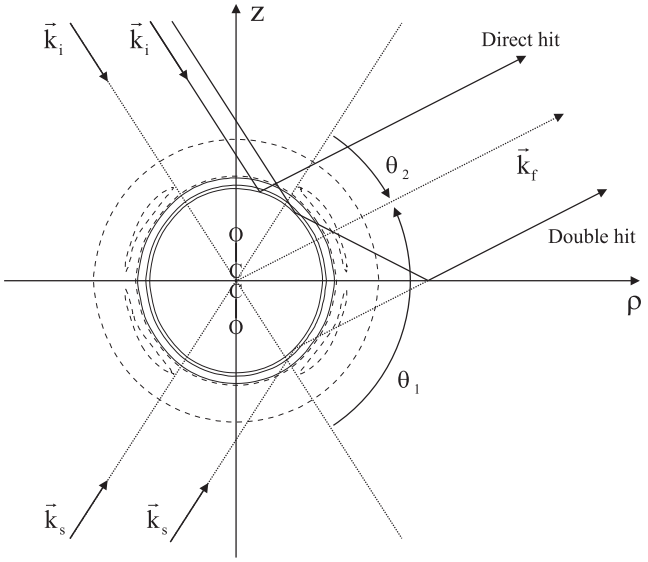

Figure 4. Schematic view of the reflection construction for $\theta_{SD} = \theta_i + \theta_f = 95.8°$, and of the classical RSI trajectories deflected by the gas phase model interaction, represented by a few energy contours in meV, calculated from the He–CO potential of Heijmen *et al* [19], with $z_{ma} = 0$. The dashed $(-1, -2.75, -1)$ equipotentials reflect the van der Waals attraction whereas the solid (0, 10, 20) ones locate the repulsive wall of the He interaction with the virtual homonuclear molecule sketched as O–CC–O.

pattern outward. The $z_{shift} = 0$ adjustable value might be a coincidence. In any case, in view of the simplicity of the interaction model it is very gratifying to obtain such a satisfactory comparison with the experiment.

We now apply the gas phase approach for completeness. The gas phase calculations were carried out with the Hibridon scattering code, version 4.1 [1], that implements the propagation algorithms of Manolopoulos and Alexander [2, 40]. The Hibridon code was slightly modified in the DCS calculation according to equation (9). Equation (10) also requires a slightly modified potential interface. The rotational constant of the virtual rigid rotor molecule was taken to be that of CO, that is 1.93 cm^{-1} [21]. The results of the simulations with $z_{ma} = 0$ are detailed in figure 6. The vertical arrows pointing to the experimental maximum positions, that are symmetric with respect to $\Delta K = 0$, pass through the calculated interference peaks. It is seen that the agreement is quite good for the first oscillation whereas the next two calculated oscillations are much too far in. A very good agreement on all three peak positions can be obtained with $z_{ma} = -0.32$ Å, which seems to be a rather significant adjustment. This is in contrast with the previous work of Lemoine [35], which did not involve any adjustment. This might originate from one of the two major qualitative differences from the present study, that is the normal-incidence geometry and the isotropic CO model. Nonetheless, qualitatively, there is no ambiguity about the relevance of the three gas phase oscillations located in the vicinity of the experimental interference maxima. Furthermore, the normal-incidence analysis demonstrates that the three first maxima have fixed ΔK positions, thereby relating to the gas phase model. Thus, we can unambiguously assign the experimental maxima as being the R_0, F_1 and F_2 peaks on both sides of the specular spike.

The gas phase formulation has the additional asset of enabling a straightforward assessment of the relevance of the RSI mechanism. This can be done by simply ignoring the constant,

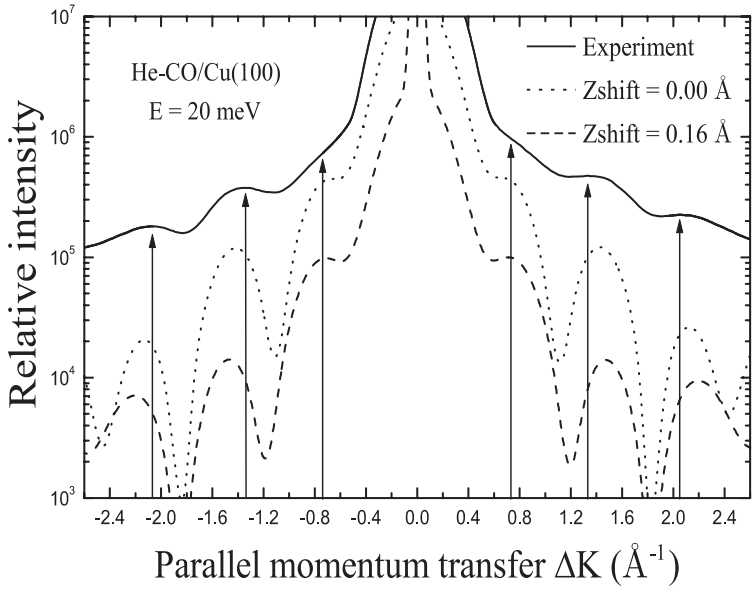

Figure 5. Log-scale plot of the angular distribution of He scattering from CO adsorbed on Cu(100), for the $\theta_{SD} = 95.8°$ geometry, at a collision energy of 20 meV. The solid curve depicts the experimental measurements of Graham *et al* [18], whereas the dotted and dashed curves refer to the pseudospectral calculations with $z_{shift} = 0$ and 0.16 Å, respectively. The vertical arrows point to the experimental maximum positions. The two arrows pointing to the near-specular shoulders are only vaguely indicative of the location of the rainbow remnant maximum.

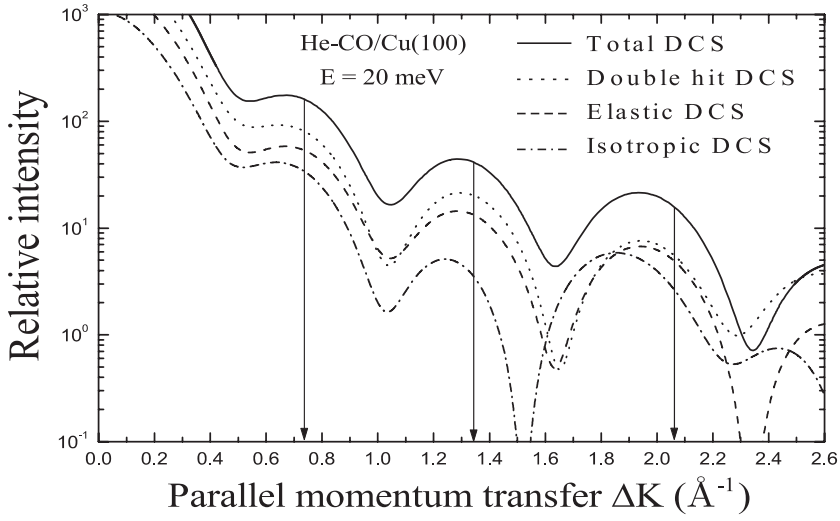

Figure 6. Log-scale plot of the DCS of He scattering from CO adsorbed on Cu(100), for the $\theta_{SD} = 95.8°$ geometry, at a collision energy of 20 meV. The gas phase model depicted in figure 4 with $z_{ma} = 0$ was used to generate all the curves. The solid curve depicts the total DCS whereas the dotted curve retains only the double-collision events and the dashed curve ignores rotational excitation. The dashed–dotted curve refers to the isotropic molecule model. The vertical arrows point to the experimental maximum positions, with the near-specular one being only vaguely indicative of the location of the rainbow remnant maximum.

direct-scattering signal, thus yielding the dotted curve in figure 6. It can be seen that there is no variation in the peak positions. Hence, the RSI mechanism plays a negligible role in the experimental distribution at a beam energy of 20 meV. In the gas phase approach the virtual molecule can fully rotate upon collision with the probe. One may question whether this rotational excitation makes sense, since the interaction model assumes a fixed adsorbate. On one hand, the rotationally inelastic DCS can be subtracted, which gives the dashed curve in figure 6. Again, no significant variation of the peak positions is noticeable. On the other hand, the potential anisotropy can be stripped off, thereby defining an isotropic adsorbate profile as in many previous studies [10, 11, 18, 29, 35]. The dashed–dotted curve illustrates the assumption of considering a virtual atomic versus molecular particle. This proves to have a quite radical effect, with the second oscillation significantly shifted inward and the third one even more. This effect has been analysed by Pack and the comparison between the solid and dashed–dotted curves is similar to that in figure 4 of [43]. If the isotropic model effectively prevents any adsorbate rotation it however modifies the probe interaction substantially.

6. Conclusions

We have reviewed and applied two distinct and realistic quantum mechanical strategies aimed at the characterization of the angular distribution of atomic scattering from a point defect inducing a corrugation much larger than that of the crystal surface. The first strategy, a quantum wavepacket approach relying on pseudospectral methods, has been detailed in both Cartesian and cylindrical coordinates. Normal-incidence simulations of He scattering from CO/Cu(100) have confirmed previous analyses of the contributing mechanisms and their energy dependence. Near-specular scattering shows a rainbow (R_0) hump induced by the He–CO van der Waals forces, and evolving as a shoulder at higher energies. Next, Fraunhofer (F_i) diffraction oscillations can be found. One important feature is the steadiness of both the R_0 and F_i maximum positions as a function of parallel momentum transfer and of collision energy. At intermediate momentum transfer the manifestation of a single-collision rainbow effect, classically occurring at a ripple in the equipotential of the turning point at the vicinity of the adsorbate, may be seen. The large deviation region is characterized by double-collision rainbow (R_i) peaks with supernumerary structures appearing at increasing energies. Those rainbows have momentum transfer positions shifting outward with increasing energy.

The second strategy is a close-coupling gas phase approach that is derived by enforcing the vanishing boundary condition along a mirror plane. It results in the difference between the scattering amplitudes for the direct scattering from the adsorbate on one hand, and for the double-collision event on the other hand. This reflection symmetry interference (RSI) formulation is quite simple and generates a virtual homonuclear molecule from the adsorbate interaction probed by the scatterer. The main qualitative weakness of this gas phase model is that the single-collision rainbow effect is not accounted for.

We have reported the first realistic comparison with the HAS experimental measurements of Graham *et al* [18] on CO/Cu(100), at a beam energy of 20 meV. The agreement obtained on the maximum positions is very good, owing to a *single* adjustable parameter. The combined use of the gas phase and of the reference models enabled us to unambiguously assign the experimental maxima as being the R_0, F_1 and F_2 peaks on both sides of the specular spike. We have also evidenced that the RSI is negligibly small in this case. Furthermore, we have shown that an isotropic gas phase model fails to reproduce the maximum positions. The dual strategy we have adopted in this preliminary HAS study of the CO/Cu(100) system has proved quite useful and needs to be pursued. Higher-energy simulations are useful to search for the double-collision rainbow presence in the experimental distributions, as well as whether to

confirm the lack of RSIs. On the other hand, the single-collision rainbow occurrence must be checked for at lower energies. Lastly, even better resolved measurements exist for the CO/Pt(111) system [8], and it would obviously be interesting to confront the results of three-dimensional pseudospectral calculations with these, and thereby to clearly assess the role of a distinct substrate.

Acknowledgments

We thank Andrew Graham and Peter Toennies for sending us their experimental data, and Ad van der Avoird for a FORTRAN subroutine of the *ab initio* He–CO potential. DL acknowledges clarifying discussions with Geert-Jan Kroes on arbitrary angles of incidence within a Fourier representation. The Centre d'Etudes et de Recherches Lasers et Applications is supported by the Ministre chargé de la Recherche, the Région Nord/Pas de Calais and the Fonds Européen de Développement Economique des Régions.

References

[1] HIBRIDON^{TM} is a package of programs for the time-independent quantum treatment of inelastic collisions and photodissociation written by Alexander M H, Manolopoulos D E, Werner H-J and Follmeg B, with contributions by Vohralik P F, Lemoine D, Corey G C, Gordon R, Johnson B, Orlikowski T, Berning A, Degli-Esposti A, Rist C, Dagdigian P, Pouilly B, van der Sanden G, Yang M, de Weerd F and Gregurick S. Home page at http://www.chem.umd.edu/physical/alexander/hibridon

[2] Alexander M H and Manolopoulos D E 1987 A stable linear reference potential algorithm for solution of the quantum close-coupled equations in molecular scattering theory *J. Chem. Phys.* **86** 2044–50

[3] Beneventi L, Casavecchia P and Volpi G G 1986 High-resolution total differential cross sections for scattering of helium by O_2, N_2, and NO *J. Chem. Phys.* **85** 7011–29

[4] Bertino M, Ellis J, Hofmann F, Toennies J P and Manson J R 1994 High resolution helium scattering studies of inelastic interferences structures of the frustrated translational mode of CO on Cu(001) *Phys. Rev. Lett.* **73** 605–8

[5] Besprozvannaya A and Tannor D J 1991 Fast sine/cosine transform for periodic functions with reflection symmetry *Comput. Phys. Commun.* **63** 569–77

[6] Carré M-N and Lemoine D 1994 Fully quantum study of the 3D diffractive scattering of He from isolated CO adsorbates on Pt(111) *J. Chem. Phys.* **101** 5305–12

[7] Chizmeshya A and Zaremba E 1992 The interaction of rare gas atoms with metal surfaces: a scattering theory approach *Surf. Sci.* **268** 432–56

[8] Choi B H, Graham A P, Tang K T and Toennies J P 2000 Helium atom scattering from isolated CO molecules on a Pt(111) surface: experiment versus close-coupling calculations for a realistic He–CO potential *J. Chem. Phys.* **112** 10 538–47

[9] Choi B H, Graham A P, Tang K T and Toennies J P 2001 Correlation between elastic and inelastic atom scattering from single adsorbed molecules *J. Chem. Phys.* **114** 2883–6

[10] Choi B H, Tang K T and Toennies J P 1997 Interpretation of helium atom scattering from isolated CO molecules on copper (001) based on an exact quantum mechanical model *J. Chem. Phys.* **107** 1631–3

[11] Choi B H, Tang K T and Toennies J P 1997 Quantum-mechanical scattering from a rigid hemisphere on a flat surface *J. Chem. Phys.* **107** 9437–46

[12] Dai J and Zhang J Z H 1996 Time-dependent wavepacket approach to state-to-state reactive scattering and application to H+O_2 reaction *J. Phys. Chem.* **100** 6898–903

[13] Dickinson A S and Certain P R 1968 Calculation of matrix elements for one-dimensional quantum-mechanical problems *J. Chem. Phys.* **49** 4209–11

[14] Ellis J, Hermann K, Hofmann F and Toennies J P 1995 Experimental determination of the turning point of thermal energy helium atoms above a Cu(001) surface *Phys. Rev. Lett.* **75** 886–9

[15] Feit M D, Fleck J A Jr and Steiger A 1982 Solution of the Schrödinger equation by a spectral method *J. Comput. Phys.* **47** 412–33

[16] Fornberg B 1996 *A Practical Guide to Pseudospectral Methods* (Cambridge: Cambridge University Press)

[17] Gottlieb D and Orszag S A 1977 *Numerical Analysis of Spectral Methods: Theory and Applications* (Philadelphia: SIAM)

[18] Graham A P, Hofmann F, Toennies J P and Manson J R 1996 Helium atom scattering from isolated CO molecules on copper(001) *J. Chem. Phys.* **105** 2093–8
[19] Heijmen T G A, Moszynski R, Wormer P E S and van der Avoird A 1997 A new He–CO interaction energy surface with vibrational coordinate dependence. I. *Ab initio* potential and infrared spectrum *J. Chem. Phys.* **107** 9921–8
[20] Heuer M and Rice T M 1985 Theory of diffuse atom scattering from isolated adatoms *Z. Phys.* B **59** 299–309
[21] Huber K P and Herzberg G 1979 *Molecular Spectra and Molecular Structure. IV. Constants of Diatomic Molecules* (New York: Van Nostrand Reinhold)
[22] Jónsson H, Weare J H and Levi A C 1984 Light atom scattering from adsorbates at low coverage *Surf. Sci.* **148** 126–38
[23] Kosloff D and Kosloff R 1983 A Fourier method solution for the time dependent Schrödinger equation as a tool in molecular dynamics *J. Comput. Phys.* **52** 35–53
[24] Kosloff R 1988 Time-dependent quantum-mechanical methods for molecular dynamics *J. Phys. Chem.* **92** 2087–100
[25] Kosloff R 1993 The Fourier method *Numerical Grid Methods and their Applications to Schrödinger Equation (NATO ASI Series C vol 412)* ed C Cerjan (Dordrecht: Kluwer) pp 175–94
[26] Kosloff R and Cerjan C 1984 Dynamical atom/surface effects: quantum mechanical scattering and desorption *J. Chem. Phys.* **81** 3722–9
[27] Kosloff R and Kosloff D 1986 Absorbing boundaries for wave propagation problems *J. Comput. Phys.* **63** 363–76
[28] Kroes G J and Mowrey R C 1994 Calculations on rotationally and diffractionally inelastic molecule–surface scattering for arbitrary angles of incidence: a new wavepacket technique *J. Chem. Phys.* **101** 805–13
[29] Lahee A M, Manson J R, Toennies J P and Wöll Ch 1987 Helium atom differential cross sections for scattering from single adsorbed CO molecules on a Pt(111) surface *J. Chem. Phys.* **86** 7194–203
[30] Lemoine D 1994 The finite basis representation as the primary space in multi-dimensional pseudospectral schemes *J. Chem. Phys.* **101** 10 526–32
[31] Lemoine D 1994 Optimal treatment of diffraction coordinates in wavepacket scattering from surfaces *J. Chem. Phys.* **101** 4343–9
[32] Lemoine D 1994 The discrete Bessel transform algorithm *J. Chem. Phys.* **101** 3936–44
[33] Lemoine D 1996 Nonreactive atom/molecule–surface scattering within the finite basis wavepacket method *Comput. Phys. Commun.* **97** 331–44
[34] Lemoine D 1997 Optimal cylindrical and spherical Bessel transforms satisfying bound state boundary conditions *Comput. Phys. Commun.* **99** 297–306
[35] Lemoine D 1998 Atomic scattering from single adsorbates: what can we learn from the gas phase? *Phys. Rev. Lett.* **81** 461–4
[36] Lemoine D 1998 Comment on 'Quantum-mechanical scattering of an atom from a rigid hemisphere on a flat surface' *J. Chem. Phys.* **107** 9437
1997 *J. Chem. Phys.* **109** 6502–3
[37] Lemoine D and Corey G C 1990 Close-coupled wavepacket calculations of the direct inelastic scattering of NO($X^2\Pi$) from Ag(111) *J. Chem. Phys.* **92** 6175–89
[38] Lemoine D and Jackson B 2001 Quantum wavepacket approach to the Eley–Rideal reactive scattering between a gas phase atom and an adsorbate *Comput. Phys. Commun.* **137** 415–26
[39] Levine R D and Bernstein R B 1987 *Molecular Reaction Dynamics and Chemical Reactivity* (New York: Oxford University Press)
[40] Manolopoulos D E 1986 An improved log derivative method for inelastic scattering *J. Chem. Phys.* **85** 6425
[41] Meyer R 1970 Trigonometric interpolation method for one-dimensional quantum-mechanical problems *J. Chem. Phys.* **52** 2053–9
[42] Muckerman J T 1990 Some useful discrete variable representations for problems in time-dependent and time-independent quantum mechanics *Chem. Phys. Lett.* **173** 200–5
[43] Pack R T 1978 Anisotropic potentials and the damping of rainbow and diffraction oscillations in differential cross sections *Chem. Phys. Lett.* **55** 197–201
[44] Périé J and Jolicard G 1993 A spectral analysis method using the optical potential as a wave absorber *J. Phys. B: At. Mol. Opt. Phys.* **26** 4491–502
[45] Persson M and Jackson B 1995 Flat surface study of the Eley–Rideal dynamics of recombinative desorption of hydrogen on a metal surface *J. Chem. Phys.* **102** 1078–93
[46] Petrella G 1990 Atom scattering from ordered structures of adsorbates on surface *Chem. Phys.* **144** 179–87
[47] Riss U V and Meyer H-D 1996 Investigation of the reflection and transmission properties of complex absorbing potentials *J. Chem. Phys.* **105** 1409–19

[48] Skorupka C W and Manson J R 1990 Inelastic scattering from Einstein modes of surface defects *Phys. Rev.* B **41** 9783–9

[49] Tal-Ezer H and Kosloff R 1984 An accurate and efficient scheme for propagating the time dependent Schrödinger equation *J. Chem. Phys.* **81** 3967–71

[50] Tang K T and Toennies J P 1992 The damping function of the van der Waals attraction in the potential between rare gas atoms and metal surfaces *Surf. Sci. Lett.* **279** L203–6

[51] Thomas L D, Kraemer W P and Diercksen G H F 1980 Rotational excitation of CO by He impact *Chem. Phys.* **51** 131–9

[52] Yinnon A T, Kosloff R and Gerber R B 1984 Time-dependent wavepacket calculations of atom scattering from surfaces with impurities *Chem. Phys.* **87** 441–9

[53] Yinnon A T, Kosloff R and Gerber R B 1988 Atom scattering from isolated adsorbates on surfaces: rainbows, diffraction interferences, and trapping resonances *J. Chem. Phys.* **88** 7209–20

[54] Zhang D H, Wu Q and Zhang J Z H 1995 A time-dependent approach to flux calculation in molecular photofragmentation: vibrational predissociation of HF–DF *J. Chem. Phys.* **102** 124–32